MICROSCOPY RESEARCH AND TECHNIQUE 00:00–00 (2015)

An Automated Imaging System for Radiation Biodosimetry

GUY GARTY,[1]* ALAN W. BIGELOW,[1] MIKHAIL REPIN,[2] HELEN C. TURNER,[2] DAKAI BIAN,[3]
ADAYABALAM S. BALAJEE,[2] OLEKSANDRA V. LYULKO,[1] MARIA TAVERAS,[2] Y. LAWRENCE YAO,[3] AND
DAVID J. BRENNER[2]
[1]*Department of Radiation Oncology, Radiological Research Accelerator Facility, Columbia University, Irvington, New York 10533*
[2]*Department of Radiation Oncology, Center for Radiological Research, Columbia University, New York, New York 10032*
[3]*Department of Mechanical Engineering, Columbia University, New York, New York 10027*

KEY WORDS dicentrics; mBAND; γ-H2AX; micronuclei; fluorescence microscopy; sCMOS

ABSTRACT We describe here an automated imaging system developed at the Center for High Throughput Minimally Invasive Radiation Biodosimetry. The imaging system is built around a fast, sensitive sCMOS camera and rapid switchable LED light source. It features complete automation of all the steps of the imaging process and contains built-in feedback loops to ensure proper operation. The imaging system is intended as a back end to the RABiT—a robotic platform for radiation biodosimetry. It is intended to automate image acquisition and analysis for four biodosimetry assays for which we have developed automated protocols: The Cytokinesis Blocked Micronucleus assay, the γ-H2AX assay, the Dicentric assay (using PNA or FISH probes) and the RABiT-BAND assay. *Microsc. Res. Tech. 00:000–000, 2015.* © 2015 Wiley Periodicals, Inc.

INTRODUCTION

Automated microscopy is an important integral component in high-content screening (Haney et al., 2006), high-throughput diagnostics and pathology (Bueno et al., 2014). In recent years the Columbia Center for High Throughput Minimally Invasive Radiation Biodosimetry has developed the RABiT (Rapid Automated Biodosimetry Tool) (Chen et al., 2009, 2010; Garty et al., 2010, 2011; Salerno et al., 2007), an automated ultra-high throughput biodosimetry workstation. Originally designed to implement two standard biodosimetry assays, the Cytokinesis Blocked Micronucleus assay (CBMN (Fenech, 2007)) and γ-H2AX assay (Redon et al., 2009; Turner et al., 2011) in filter bottom multiwell plates. In recent years, continuous improvements and refinements have been made to expand and enhance the RABiT capabilities to include a wider range of endpoints such as the Dicentric assay (M'kacher et al., 2014; Wilkins et al., 2011), chromosome banding (mBAND) (Chudoba et al., 2004), and DNA repair kinetics (Sharma et al., 2015; Turner et al., 2014). Concurrently, we have also expanded on the use of custom-built robotics at our center and RABiT protocols are currently being developed and optimized for commercial robotic systems (Repin et al., 2014) such as Perkin Elmer's cell::explorer, originally developed for high content screening.

Expansion of RABiT technology to accommodate new automation platforms and new assays has prompted us to revamp our existing imaging system design (Garty et al., 2010, 2011). Our main motivation in these upgrades to the imaging system was not ultrahigh throughput but rather versatility in use (while maintaining reasonably high throughput, of course).

Our goal was to develop an effective imaging system which has the flexibility of rapid switching between different assays and sample types. Development of such a system obviously includes a number of considerations: (i) number of fluorochromes that may vary from one (CBMN assay) to six (mBAND assay), (ii) imaging substrates may be either cytogenetic slides or glass bottom multiwell plates, and (iii) resolution and imaging brightness may vary over a wide range depending on the assay. Here, we describe the operational development, characterization and optimization of our imaging system for high throughput automated analyses for four different biodosimetry assays.

MATERIALS AND METHODS

Overall Structure of the Imaging System

A photo and sketch of the imaging system is shown in Figure 1. The Imaging system, based on Nikon CFI60 infinity optics components, is built on a 3′ × 4′ optical breadboard table (Newport Corp., Irvine, CA), providing flexibility in design and a sturdy base. Use of infinity optics components (Sluder and Nordberg, 2007) allows inserting multiple dichroic mirrors and filters in the "infinity space" between the objective and the tube lens with minimal aberrations. The imaging system was built predominately using opto-mechanical components

---

Additional Supporting Information may be found in the online version of this article.

*Correspondence to: Guy Garty, Radiological Research Accelerator Facility, Columbia University, 136 S. Broadway, P.O. Box 21, Irvington, NY 10533, USA. E-mail: gyg2101@cumc.columbia.edu

Received 26 January 2015; accepted in revised form 11 April 2015
REVIEW EDITOR: Prof. Alberto Diaspro

Some of the reagents, equipment and plasticware used in this work were purchased through Fisher Scientific. At the time of writing this manuscript GG owns 90 shares of Thermo Fisher Scientific stock. The authors report no other potential conflicts.

Contract grant sponsor: National Institute of Allergy and Infectious Diseases (NIAID), National Institutes of Health (NIH); Contract grant number: U19-AI067773.

DOI 10.1002/jemt.22512

from Thorlabs (Newton, NJ) with non-standard components manufactured at our machine shop.

Contrary to our previous design (Garty et al., 2011), there is only one imaging path, as the use of independent cameras for each color becomes prohibitively complex (and expensive) when imaging six-color mBAND samples. This eliminates possible misalignments and small discrepancies in magnification arising due to the use of independent cameras on different imaging paths as well as minimizing possible bleed through between the different color channels, which are now imaged sequentially rather than simultaneously.

The system, shown schematically in Figure 1b, consists of three partially overlapping light paths, separated by a series of dichroic mirrors. Excitation light is delivered from the light source, described below, by a liquid light guide. It is filtered and focused to a parallel beam before bouncing off a quad-band dichroic (marked †, in the figure). It is reflected and steered using a galvanometric mirror scan head and finally focused onto the sample using one of the objectives detailed in Table 2 below.

Fluorescence light is collected by the same objective and returns along the same path to the quad band dichroic. After passing through the dichroic, the light is filtered and focused onto a scientific CMOS (Complementary Metal Oxide Semiconductor) sensor.

The third light path is used for focusing. Infrared light is provided by the CRISP (Continuous Reflective Interface Sample Placement) autofocus unit. It is parallelized and merged into the other two beam paths using a dichroic mirror (marked ‡, in the figure). The operation of the autofocus unit is described below.

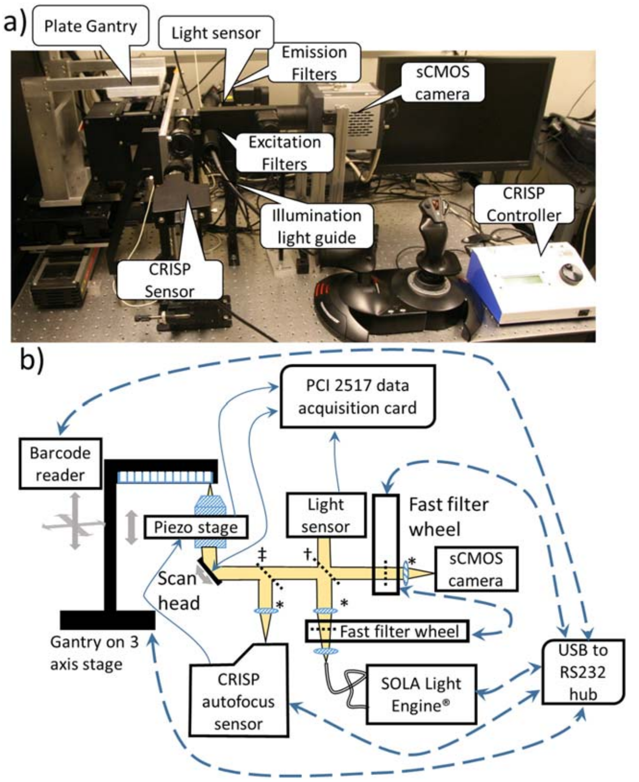

Fig. 1. (**a**) Photo and (**b**) schematic diagram of the imaging system. Each box represents a single peripheral device. Dashed thick lines correspond to RS232 communications. Thin solid lines correspond to analog control. The arrows denote the direction of communication. Thick arrows represent motion. Hashed shapes represent optics (the lenses marked with * are tube lenses (200 mm Nikon Tube lens, Edmund optics, Barrington, NJ)). The dichroic mirror marked with † is a custom quad-band dichroic mirror (475/525/600/690 QBDR, Omega Optical, Inc., Brattleboro, VT). The dichroic mirror marked with a ‡ is an infrared mirror which is part of the CRISP autofocus system. [Color figure can be viewed in the online issue, which is available at wileyonlinelibrary.com.]

Control Software

A unified, form-based control software was written in Visual C++ (Microsoft, Redmond, WA) to provide both highly interactive control of all components of the imaging system, as well as fully automated, unsupervised, imaging of up to four slides or a multiwell plate. Effort was made to use freely available libraries, whenever possible. The software was written in a modular fashion so that if a specific piece of hardware is changed only one module would need to be rewritten. The control software architecture is shown in Figure 2.

Forms were generated for the main peripherals: the mechanical stage, the sCMOS camera and the illumination system (The SOLA light engine® and the two fast filter wheels). A separate form was generated for monitoring the CRISP autofocus unit with the actual control of the unit done using the form provided by the vendor. These forms implement low level control of their respective instruments while exporting high level controls (e.g. “take 6-color picture”) and providing status information that can be queried by other forms or the user.

An additional “spiral scan” form was written to control unsupervised scanning of a sample, this form implements a scan by moving the stage in a rectangular spiral pattern, taking pictures at each location. The spiral pitch and step size are selected to be slightly larger than the field of view of the objective being used so that non-overlapping images are acquired.

Image analysis was performed either using a dedicated form in the software or using an external stand-alone program, utilizing the same routines. In addition to allowing for offline analysis of images from the imaging system, the use of a standalone program allows analysis of images from other imaging systems available in our lab.

With the exception of the camera and scan head, the software communicates with all hardware components, via the RS232 protocol. As the control PC has no built in RS232 port, an eight-port USB to RS232 hub was used (Moxa Inc., Brea, CA). In order to provide analog voltage control (required for the scan head) and to monitor the analog output of various components (as detailed below), a PCI-2517 data acquisition board (Measurement Computing, Norton, MA) was used. The camera communicates with its frame grabber (Neon-CLB, Bitflow Inc., Woburn, MA) via a dedicated cameralink cable.

Inherent in RS232 control is that it does not normally block execution of the control software, which can continue operating after issuing a command, even if the command had not finished execution (e.g. changing excitation filters typically takes 30 ms). This allows parallelized operation of many peripherals with overlapping lag times, without requiring one to finish

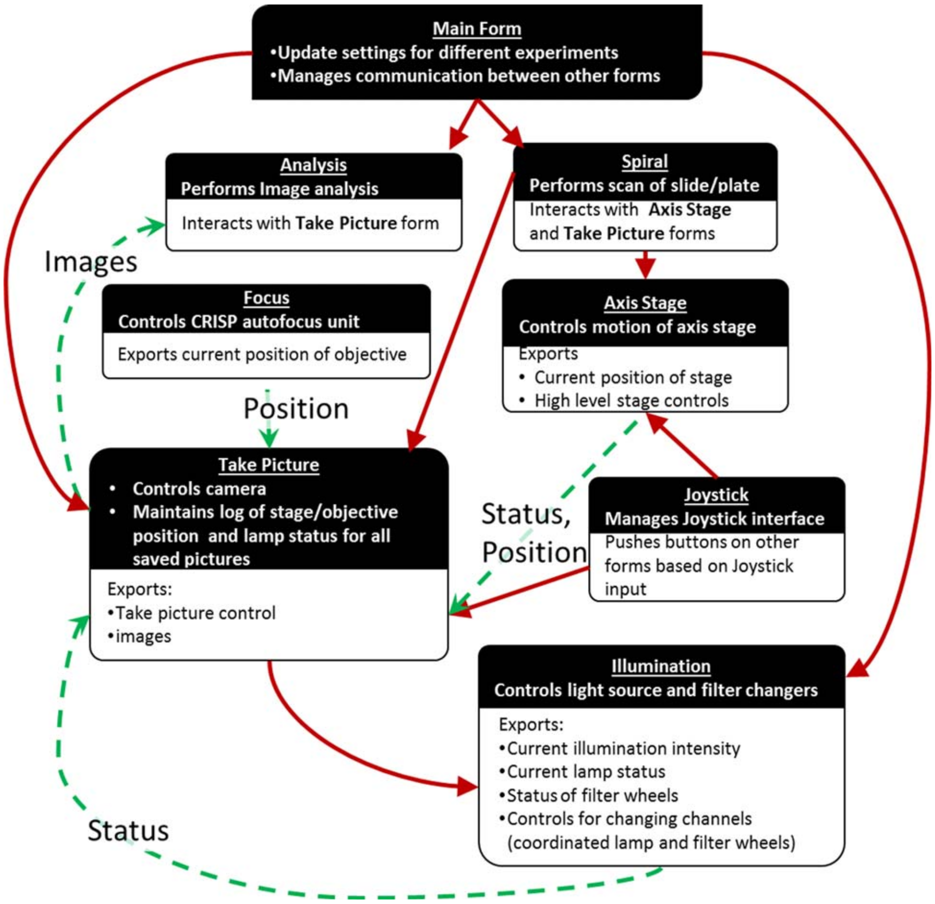

Fig. 2. Forms available in the control software.The solid arrows denote actuating a control in another form. The dashed arrows denote data transfer. The text overlayed on the dashed arrows indicate the type of data transferred. [Color figure can be viewed in the online issue, which is available at wileyonlinelibrary.com.]

before the next one is actuated. However, it requires explicit verification that the required action had finished if subsequent actions depend on it. To allow this explicit verification, we implemented a periodic monitoring of the RS232 ports for responses from the peripherals. Each peripheral's form exports one or more flags indicating whether the peripheral is busy or not. At key points in the control loop (e.g. before grabbing an image) verification is made that all prerequisite actions had completed. The only exception is the SOLA light engine® which does not report on its status. Feedback for light engine operation was therefore implemented using a light sensor (see "Illumination" below).

Sample Manipulation

In the previously described imaging system, the samples to be imaged were filter bottoms of multiwell plates, held between thin sheets of clear tape. In line with recent changes in the RABiT philosophy (Repin et al., 2014), we have modified the imaging system to allow handling of both standard cytogenetic slides and "glass-bottom" multiwell plates. Two main changes were made:

- The scan head was inverted, so that imaging is done from below rather than from above. This is done to prevent the need to invert a multiwell plate, which may contain liquid, for imaging. This mode supports air- and oil-immersion optics, but not water immersion.
- A gantry (Fig. 1) was added to the XYZ stage, previously used to hold the sample. The gantry allows suspending a single multiwell plate or a set of four slides above the objective. The XYZ stage was adjusted such that the lower Z limit (enforced by a hardware limit switch) is encountered when the bottom of the slide/plate is just barely touching the objective. In the case of the 60× oil immersion lens this corresponds to a few tens of microns closer to the objective than the focal plane.

The stage and controller remained the same as previously reported (Garty et al., 2010, 2011). To facilitate use of the stage for manual imaging, a joystick control was added, via a form that periodically queries the joystick and actuates controls on the other forms.

To accommodate for the heavier gantry and sample, the stage controller feedback parameters were retuned so that a 1 mm motion (on either axis) is completed within 60 ms).

Focus

A major rate-limiting step in modern automated microscopes is the autofocus routine. In order to get good image quality, typical microscope objective lenses have a shallow depth of field and may therefore be sensitive to the flatness of the sample being imaged. For example, some brands of multiwell plate have a 30 μm variation from the center of a well to its edges. The simple solution to this is to take several images at different object-lens distances (a Z-stack), quantify the quality of focus (QoF) and search for the best setting (Geusebroek et al., 2000; Zeder and Pernthaler, 2009). Selection of a good QoF function depends greatly on the type of image being investigated and, although much work has been done on finding the optimal quantifier for the quality of focus (Liu et al., 2007), the method remains inherently slow due to the necessity of grabbing multiple images. Depending on the implementation, there is also a possibility that the system escapes from focus if there are no cells in the field of view, causing at best a long lag and at worst loss of several subsequent frames while focus is reestablished.

In previous work (Garty et al., 2011), we have investigated the use of cylindrical optics in a secondary beam path to quantify distance to focus from a single image but have not found the method reliable enough for chromosome imaging. An alternate commercial solution is now being offered by several vendors. The CRISP system (Continuous Reflective Interface Sample Placement, Applied Scientific Instruments, Eugene, OR) and a similar system from Nikon, maintain focus by projecting IR light onto the sample, through half of the objective aperture. The image, reflected off the surfaces where refractive index changes (e.g. the boundary between the sample and the substrate), will move laterally across the CRISP sensor as focus is changed, allowing a quantitative evaluation of focus position (called the "error value," Fig. 3). The controller implements a hardware feedback loop to maintain a preset error value and hence consistent focus by adjusting the objective position. The CRISP system also provides for real time adjustment of the focus position via an external knob on the controller, which varies the target error value.

Although the CRISP system does not actually focus on the sample but rather on the cover slip or slide surfaces, it is possible to adjust the relative distance of the camera and CRISP unit from the tube lens to ensure that while the CRISP is focused on the cover slip, the camera is focused on the cells/chromosomes to be imaged.

We have incorporated a CRISP system as shown in Figure 1. Although the vendor recommends placing the CRISP beam splitter immediately before the camera we have found it more convenient to place it in the infinity space between the main dichroic and the scan head. A Nikon tube lens (Edmund Optics) was placed between the CRISP unit and the scan head replicating the optics path of the imaging light path.

As before, we mounted our objective lens on a 100 μm piezo actuator (OP-100, Mad City Labs, Madison, WI) which was directly controlled by the CRISP control hardware. An integrated sensor on the piezo actuator was continuously monitored by the control software. Figure 3 shows the typical error value of the CRISP system as a function of objective position. The capture zone (the region between the maximum and minimum) is about 20 μm for the 60× lens and about 60 μm for the 20× lens. The CRISP will maintain focus as long as the objective-sample distance is within this range. If it is outside this range, the CRISP will drive the objective to the end-of-travel for the piezo actuator. This deviation from the normal position of the piezo actuator (typically set to the middle of its range) is detected by the control software and the operator is alerted.

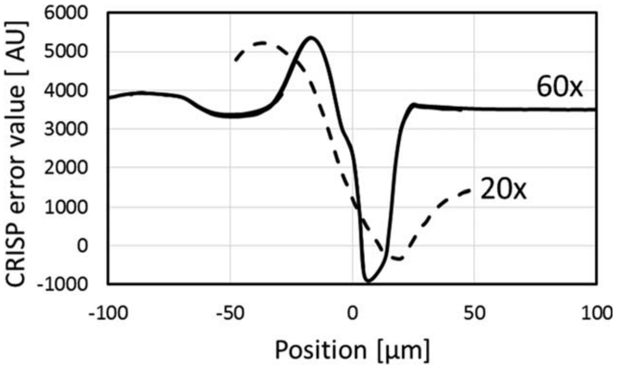

Fig. 3. Error value of the CRISP unit as function of objective lens position above or below focus. The dashed line corresponds to our 20× lens. The solid line, stitched from four overlapping 100 μm scans, corresponds to the 60× lens.

Illumination

The Illumination light path needs to deliver, at the back aperture of the objective, a uniform, bright beam at each of six wavelengths, corresponding to optimal excitation of DAPI (4',6-diamidino-2-phenylindole), DEAC (diethylaminocoumarin), FITC (Fluorescein isothiocyanate), Spectrum Orange, Texas Red and Cy5 (Cyanine), the standard mBAND fluorochrome-tagged probes. Conventional chromosome imaging systems (e.g. the ones offered by Applied Spectral Imaging and by MetaSystems) use a bright mercury lamp and standard microscope filter cubes, which results in slow switching between wavelengths, potential crosstalk between the channels (as all excitation wavelengths enter the cubes at all times) and extremely inefficient excitation of Cy5, which requires excitation at ~650 nm, not efficiently available from a Hg-lamp.

Over the past few years several new LED-based "light engines" have emerged for fluorescence microscopy. These light sources are not as bright as the standard Hg-based arc lamps but much more versatile. They require less power, generating less heat and thermal distortion of the microscope, have a much longer lifetime, but, more importantly, they allow rapid wavelength switching under RS232 or TTL control. This makes them particularly attractive for automated microscopy. The imaging system we have developed makes use of an early model of the SOLA light engine® (Lumencor Inc. Beaverton, OR) which provides independent RS232 control of six LEDs.

Figure 4 shows a comparison of the light generated by the six LEDs to the light of a commercial mercury-based lamp (Excite 120PC, Exfo life Science, Toronto,

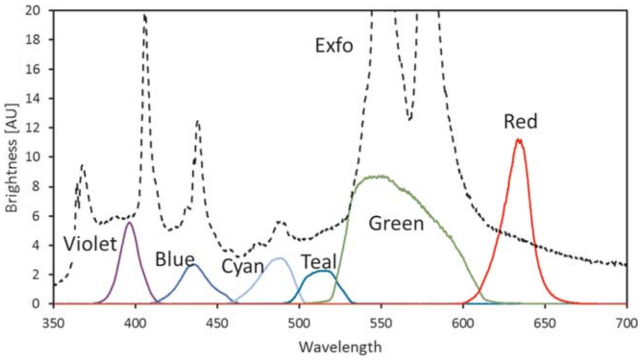

Fig. 4. Comparative spectra of the 6 independently controlled LEDs in the SOLA light engine® (solid lines) and an EXFO 120PC Hg lamp (dashed line, bulb timer: 1002 h), measured under identical conditions using an SPM-002-C spectrometer (Photon Control Inc.). [Color figure can be viewed in the online issue, which is available at wileyonlinelibrary.com.]

ON, Canada; bulb timer: 10:02 h). Although the spectral lines from the SOLA light engine® do not in some cases match up to those of a mercury lamp (in particular there is no bright LED at 366 nm), they are sufficiently close to excite standard fluorochromes. Furthermore, the SOLA light engine® provides a red excitation light, useful for exciting stains like Cy5.

The light is delivered to the imaging system via a liquid light guide. A parallel beam is generated with a 40 mm singlet lens (Thorlabs) followed by an additional 200 mm Nikon Tube lens (Edmund Optics) and filtered by one of six excitation filters mounted in a fast filter changer (HS-625, Finger Lakes instrumentation, Lima, NY). After filtering the illumination light is reflected into the main optic axis using a custom quad band dichroic filter (475/525/600/690 QBDR, Omega Optical, Inc., Brattleboro, VT). On the return, imaging, light path a second HS-625 fast filter changer (Finger Lakes Instrumentation) is placed between the dichroic mirror and the downstream tube lens to filter out stray excitation light from the illumination path.

We have tried operating the system without excitation filters but observed that there is some crosstalk between the illumination and imaging light paths, due to the relatively broad spectra of some of the LEDs. The excitation and emission filters (Table 1) were chosen as an optimization between the peak intensity of the LEDs, the peak excitation efficiency of the fluorochromes and the peak reflection/transmission bands of the quad-band dichroic used to separate excitation and emission light. Note that the Green LED has a very broad spectrum and is thus used to excite two stains, through different excitation filters.

Residual light passing through the dichroic filter is collected by a Si Transimpedence Amplified Photodiode (PDA100A; Thorlabs) which is used to monitor a proportion of the intensity of the illumination light. The sensor typically provides a voltage of 5 to 10 V (using the 0 dB setting) when the lamp is on and the LED is matched to the excitation filter and <0.1 V otherwise. This provides a good verification for the proper actuation of the lamp LED selection and the filter changer position.

Imaging

Imaging is performed using an Andor Neo 5.5 sCMOS camera (Morrell Instruments, Melville, NY). sCMOS technology (Fowler et al., 2010) provides low noise ($\sim 1e^-$) and high signal to noise ratio, as well as fast imaging and data transfer rates (100 fps). This camera provides a cooled 1" sensor with a resolution of up to 2,560 × 2,160 and a pixel size of 6.5 μm. In the applications described below, exposure times between 50 and 1,500 ms were used, depending on the stain. The sCMOS camera was operated in 16-bit "low noise, high well capacity" mode (Fowler et al., 2010) and the image was cropped "in camera" to 1,776 × 1,760 pixels (see below).

Alignment

Alignment of the camera relative to the optics path was verified by operating the camera at full resolution and centering the crop pattern of the emission filter on the sensor, while imaging the room lights through the optics path. When all optics are aligned, the four corners of the image are occluded symmetrically. Once the camera was aligned, it was locked into position using 1" extruded aluminum rails (Thorlabs).

Alignment and focusing of the illumination source was monitored by replacing the objective with a frosted glass alignment disk (DG10-1500-H1, Thorlabs) and verifying that the illumination beam is centered on and is slightly larger than the objective's back aperture.

Image Analysis

All image handling and processing was performed using the OpenCV imaging library (version 2.4.6, www.opencv.org).

Raw images were obtained from the camera as (*unsigned char **) arrays. They were cast to 16-bit

TABLE 1. Excitation and emission filters used for the various fluorochromes

Fluorochrome	Peak excitation (nm)	Peak emission (nm)	LED "name"[a]	Excitation filter[b]	Emission filter[c]
DAPI	358	461	Violet	400/40	450/65
DEAC	432	472	Blue	445/20	480/30
FITC	495	519	Cyan	482/35	530/30
Spectrum Orange	559	588	Green	543/22	580/30
Texas Red	595	620	Green	585/29	620/35
Cy5	649	670	Red	643/20	682/22

[a] See Figure 4 for spectrum.
[b] Semrock, Rochester, NY.
[c] Omega Optical Inc. Brattleboro, VT.

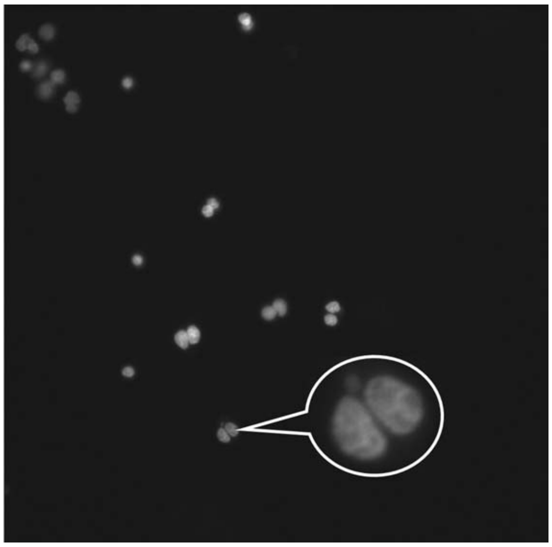

Fig. 5. Image obtained from one-color micronucleus assay in a multiwell plate. Binucleated cells and a micronucleus are visible within one 40× frame (1,776 × 1,760 pixels).

(*unsigned __int16* *) arrays and loaded into appropriate OpenCV *Mat* structures.

Several of the OpenCV routines cannot handle the 16-bit images generated by the camera. The display routine (*imshow*), for example, only displays the lower 8 bits of an image. The adaptive threshold routine also requires 8-bit images. To overcome this, background-subtracted images were down-sampled to 8 bits by locating the brightest pixel value, V, in the image and dividing all other pixels by $f = V/255$. This forms an 8-bit image with the minimal possible reduction in dynamic range. The down-sampling factor, f, is made available to the integrated analysis routines in order to allow quantitative fluorescence measurements. In any case the images saved to disk are the raw 16-bit images with a separate uncompressed TIFF file generated for each fluorophore. File names are automatically constructed from the channel name and a sequential index, with zero usually corresponding to a background image. This facilitates batch analysis of the images by the offline software. During automated imaging, images are saved to disk only if the brightest pixel is larger than a specified threshold value (typically 500 on a scale of 0-65536). An optional second image at reduced bit depth and including background subtraction and/or gain corrections can also be saved, under a different filename.

A live view mode, where images are continuously grabbed disregarding the state of all other peripherals, was provided to facilitate setup for automated imaging and can also be used for manual image capture. In live view, a digital zoom function was also provided.

Sample Preparation

The images shown below were obtained from multiwell plates and slides generated in the routine testing, development and optimization of RABiT protocols. As the RABiT is currently configured for performing the micronucleus assay we used it to generate the plate imaged for Figure 5. The γ-H2AX assay (Fig. 6) was performed in the conventional method, using 15 mL tubes and a cytospin cell preparation system (Thermo Fisher Scientific). The dicentric and mBAND assays (Figs. 7 and 8) were performed in multiwell plates, using the protocol intended for implementation on the RABIT II system (Repin et al., 2014).

A detailed description of the preparation of the samples is given in the Supporting Information.

RESULTS

We have developed this imaging system to serve as the last stage of the RABiT automated biodosimetry tool (Garty et al., 2011; Repin et al., 2014). Within that framework, four biodosimetry assays have been developed. Here we present a brief description of the imaging requirements for each assay and demonstrate typical images obtained. For further information, the reader is referred to our previous papers (Lyulko et al., 2014; Turner et al., 2011) which describe the γ-H2AX and micronucleus analysis algorithms in detail with a more comprehensive data set. As the manuscript describing the chromosome based analysis is still in preparation, we provide more details on these assays.

Assay 1: Micronuclei

The Cytokinesis Blocked Micronucleus (CBMN) assay (Fenech, 2007; IAEA, 2011) is one of the earliest reliable and most recognized biodosimetry assays. This assay quantifies radiation-induced chromosome damage expressed as postmitotic micronuclei. In this assay, lymphocytes are stimulated to undergo proliferation and nuclear division but ensuing cytokinesis is blocked with Cytochalasin B leading to the formation of binucleate cells. Healthy lymphocytes form binucleate cells, while those with chromosome damage can form an additional micronuclei encompassing chromosomal fragment(s) and the frequency of binucleate cells with micronuclei increasing monotonically with dose. A key advantage of the micronucleus assay is that the signal is stable for many months postexposure (da Cruz et al., 1994).

The imaging requirements for this assay are relatively modest, two imaging channels are required (nuclear stain and cytoplasmic stain) although with proper cell density in slide preparation, the cytoplasmic staining is not required and cells can be identified by the proximity of their constituent nuclei, as seen in Figure 5.

The resolution provided by our imaging system at 40× is sufficient to both separate adjacent nuclei in one binucleate cell and to reliably detect micronuclei.

Image analysis is performed by locating the nuclei, using a custom designed thresholding algorithm (Lyulko et al., 2014). Each nucleus is correlated with a cell and the number of nuclei of different sizes within a cell are scored. Cells with serrated or abnormal nuclear morphology are rejected from the analysis.

Assay 2: Immunocytochemistry

Histone H2AX is rapidly phosphorylated at serine 139 in response to radiation exposure and phosphorylated H2AX (γ-H2AX) molecules form foci at or near the vicinity of DNA double strand breaks (DSB)

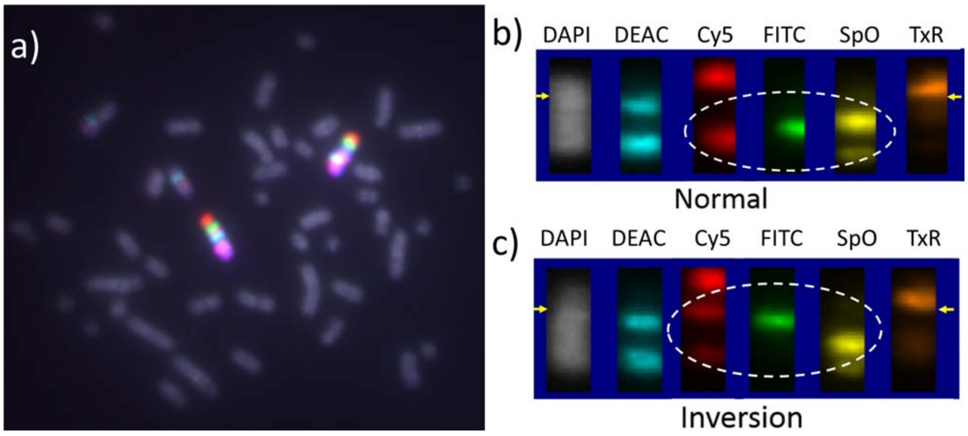
a)
b)
DAPI
DEAC
Cy5
FITC
SpO
TxR
Normal
c)
DAPI
DEAC
Cy5
FITC
SpO
TxR
Inversion

(Rothkamm and Löbrich, 2003). γ-H2AX foci are detected by indirect immunostaining and quantified by fluorescence intensity relative to unirradiated control cells (Rothkamm and Löbrich, 2003). Under the manual procedure, the yield of phosphorylated H2AX is quantified by counting foci at high magnification (Mariotti et al., 2013). Several automation systems based on counting foci have been described in the literature (Hou et al., 2009; Valente et al., 2011) but they require acquisition of Z-stacks and high resolution imaging. Although very sensitive at low doses, the foci counting technique is less appropriate for higher doses, due to foci overlap, resulting in reduced foci counting efficiency at doses of 2 Gy or more (Böcker and Iliakis, 2006). The applications of interest in our center revolve around higher doses in the 2-6 Gy range, both for radiological triage (Turner et al., 2011) and for investigations of DNA repair capacity across populations (Sharma et al., 2015).

We therefore use an alternate technique for quantifying H2AX phosphorylation (Turner et al., 2011). Two fluorescent images are taken (one of the DAPI-stained nucleus and one of the γ-H2AX-bound fluorescent antibody). Nuclei are identified from the DAPI-stained image and the fluorescent intensity in the nucleoplasm is integrated and scored. This allows the use of much lower magnification, resulting in both higher throughput (fewer images) and greatly increased depth of field. Using this technique we have seen a linear response up to at least 8 Gy with sensitivity around 0.3 Gy.

As an example Figure 6 shows the captured images of cells irradiated with 4 Gy, using our system at various magnifications. The upper row shows a full frame image (1,760 × 1,776) demonstrating typical cell yields in each field of view where the bottom row shows an additional 10× expansion demonstrating image quality for individual cells. As described by Turner et al. (2011), the analysis software performs a background subtraction based on the fluorescence intensity in the immediate area of the cell. We have experimented with imaging using 60× oil, 40× air, 20× air, and 10× air objectives and observed good correlative results with all magnifications. The 20× air objective is particularly useful due to the larger field of view (0.6×0.6 mm^2), so that sufficient number of cells required for analysis could be obtained with a fewer image fields. Although the resolution of the 10× image does not allow detection of individual foci, the image quality is sufficient to discriminate between valid (round) and apoptotic cells and perform a quantitative fluorescence measurement. As can be seen, in Figure 6, the 10× image suffers from misalignment of the two images, either due to chromatic aberration or due to pixel shift in the emission filters (Erdogan, 2011). Subsequently, much of the antibody fluorescence is imaged outside the nuclear boundaries, although this can be corrected for, by realigning the images during analysis. Similar assays have been developed in our lab for other proteins (Sharma et al., 2015; Turner et al., 2014).

Assay 3: Dicentric Analysis

For many decades, the dicentric chromosome assay has been the "gold standard" for radiation biodosimetry, because ionizing radiation is fairly specific for inducing dicentric chromosomes. It has been used in every major radiological incident over the past 30 years, including Fukushima (Lee et al., 2012). Historically, this assay is based on morphologic image analysis of Giemsa (Romm et al., 2013) or DAPI (Rogan et al., 2014) stained metaphase spreads, which have defied useful rapid automation, due to issues of background, shape variation, and chromosome overlap.

Several approaches to morphometric detection of dicentric chromosomes are available. However, they are computationally difficult, requiring parallel computing to achieve any reasonable throughput (Rogan et al., 2014). An alternative technique under development by us and others (M'kacher et al., 2014) is the use of FISH or PNA probes specific for centromeres and telomeres of all human chromosomes. In this case, dicentric detection becomes relatively easy, one needs to score the chromosomes with 0, 1, or 2 bright centromeric spots as shown in Figure 7.

Within our imaging system, three images are taken, corresponding to the DAPI-stained chromosomes, the Centromere Marker and the Telomere marker (Fig. 7a shows a composite picture of the three images). The analysis software identifies each chromosome, based on the DAPI signal. This is done by first binarizing the background-subtracted DAPI image using an adaptive threshold algorithm, which assigns each pixel a value of 1 if its value is significantly larger than pixels in a 99×99 pixel neighborhood and zero otherwise. Chromosomes are then located as Binary Large Objects (BLOBs), using the algorithm of Suzuki and Abe (1985). BLOBS within a size range of 100 to 5,000 pixels (corresponding to 1–50 μm^2) and having an aspect ratio greater than 2 are selected for further analysis.

The software then extracts the corresponding regions from the other two images (Fig. 7b), and integrates the images laterally generating a brightness profile (Fig. 7c). Brightness maxima exceeding designated thresholds are located for each profile. The number of peaks along this profile is scored for each channel. A normal chromosome will have two telomeric peaks surrounding a centromeric peak, whereas a dicentric will have two centromeric peaks.

The imaging requirement for this assay are much more stringent than for the γ-H2AX and micronucleus assays, because a 60× oil immersion lens is required for precise detection of both chromosome arms and the fluorescence dots which in most cases are not extremely bright.

Assay 4: mBAND

The mBand assay is a well-established technique for scoring intra chromosomal rearrangements (Chudoba et al., 2004). It consists of "painting" the entire chromosome length using region-specific over lapping chromosomal DNA fragments that are separately and combinatorially labeled with five different fluorophores. This results in a multicolor banded image of a single chromosome, where each band is defined by a combination of 1, 2, or 3 fluorophores. In a typical case, 11 differently colored bands can be detected along the length of human chromosome 5 using an mBAND probe set. By analyzing the sequence of chromosome bands, intra-chromosomal aberrations, which are characteristic of high LET radiations (e.g. neutrons), can be detected.

TABLE 2. Parameters of the objective lenses used in this work

Assay	Objective used	Magnification	FOV[a]	NA	Working distance	Depth of field[b]
Micronucleus	Plan Fluor 40×	40× Air	0.3 mm	0.75	0.66 mm	1.0 μm (DAPI)
Immunostaining	Plan Apo 10× λ	10× Air	1.2 mm	0.45	4.0 mm	3.7 μm (DAPI)
	Plan Apo 20×	20× Air	0.6 mm	0.75	1.0 mm	1.2 μm (DAPI)
Chromosome based assays	Apo TIRF 60× oil	60× Oil	0.2 mm	1.49	0.12 mm	0.42 μm (DAPI) 0.55 μm (Cy5)

[a] Field of view for 1,760 × 1,776 pixel cropped image. Uncropped image is 40% wider and taller.

[b] Calculated as: $\frac{n}{\mathrm{NA}}\left(\frac{\lambda}{\mathrm{NA}}+\frac{p}{M}\right)$, where λ is the wavelength, n is the refractive index, NA the numerical aperture, M the magnification, and p the camera pixel size (6.5 μm).

This assay requires acquisition of six images, corresponding to the DAPI counterstain and five different probes (DEAC, FITC, SpO, TxR, and Cy5; see Fig. 8a). The different colored images need to be aligned precisely so that the order of the bands is preserved. The initial analysis is similar to that of the dicentric assay, although it is more complicated due to the multiple stains and the requirement to detect partially overlapping regions. Here, the full-width at half maximum (FWHM) about each maximum identifies the bounds for that probe band. To facilitate analysis, each combination of probes along the length of the chromosome is assigned a unique character, generating a string corresponding to that chromosome's peak structure. The string is then compacted by removing blanks (regions with no probe), duplicate consecutive characters (compacting each band to a single character) and isolated characters (which may be due to sporadic noise). Scoring is performed by comparing the order of bands detected with the "standard" order for that chromosome. For example, Figure 8b shows the banded pattern for a normal chromosome (software generated string: PXHAEDFBSQU) and Figure 8c shows the altered banding pattern of a damaged chromosome (software generated string: PXHQSBFDEAU) showing a paracentric inversion induced by neutron radiation. Note that the seven-band section underlined is simply reversed with respect to the normal chromosome.

DISCUSSION

Choice of Objective and Required Statistics

The choice of objective for each experiment (Table 2) is dictated by a balance of the required resolution with the need for a large field of view to allow collection of maximal statistics from a minimal number of images. Depending on the assay and required precision, the number of scoreable cells needed for analysis can range from 50 (Lloyd et al., 2000; Turner et al., 2011; Wilkins et al., 2011) to 1,000 (Fenech et al., 2003). In order to achieve these statistics within a short span of time, the lowest possible magnification should be used. While this may not be possible for chromosome-based assays which require a higher magnification (60×) to identify submicron spots on chromosomes, immunofluorescence-based assays are more flexible, as the required resolution is limited by the need to identify round nuclei, which can be easily done at 10× or 20×. Consequently, while a good chromosome preparation will contain a single scoreable metaphase every few 60× frames a good immunostaining preparation may contain tens of scoreable nuclei per 20× frame.

In the case of the Micronucleus assay, typical micronuclei have a diameter of about a micron and need to be reliably detected. Given the 6.5 μm pixel size of the camera, it is clear that in images taken with a 10× lens, small micronuclei may not be detected reliably, resulting in reduced yields. This can be taken into account using the calibration curve of the system but may result in lower sensitivity and precision. A 40× air lens is typically used in our lab for this type of imaging although others have reported the use of 10× (Varga et al., 2004) or 60× objectives

A second consideration is the Numerical Aperture (NA) of the objective, which determines both the depth of field and the amount of light passing through the lens. Using high NA lenses results in much faster imaging as the same level of contrast can be achieved using shorter exposures. However, the use of high NA objectives poses some challenges in system construction. As NA is inversely related to the working distance of the objective (see Table 2), the objective needs to be placed close to the sample.

This poses a challenge particularly for the 60× oil objective, with a working distance of 120 μm. The sample holder must be designed such that there is no material protruding below the imaging substrate. Any protrusion risks damaging the objective when the sample is moved between fields of view or between different samples on adjacent slides or in adjacent wells. As the increased image brightness and enhanced resolution provided by this objective (as compared with a standard 60× air lens) is crucial for rapid imaging of subchromosomal regions, we have made an effort to design the sample holder to accommodate such a short working distance.

For multiwell plates, the gantry was designed to hold the plate from above so that only the skirt of the plate protrudes below the plate surface. This is not possible with cytogenetic slides, which must be held from below, so a slide holder was manufactured that protrudes below the slides only at the very edge of the slide, only by about 100 μm. This allows access to the entire imaging area of all four slides.

Focusing

Numerical aperture and magnification also determine the depth of field, which is the precision with which the system needs to be focused. For assays such as the micronucleus and chromosome-based assays, the main requirement on focusing is that the small objects imaged be discernible.

For immunostaining assays, there is a concern that an out of focus image would result in a lower

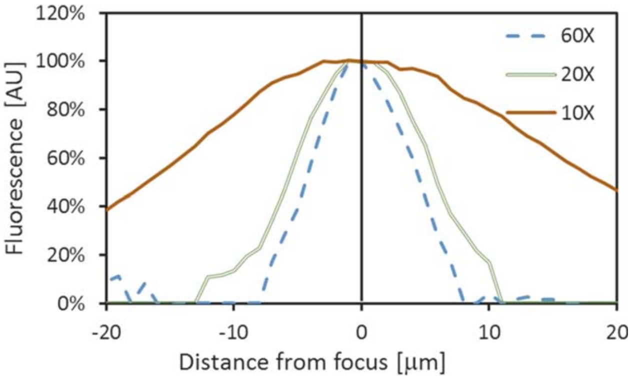

Fig. 9. γ-H2AX yields as a function of distance from focus for different lenses. [Color figure can be viewed in the online issue, which is available at wileyonlinelibrary.com.]

fluorescence yield. However, as long as all fluorescence light is collected, the measured fluorescence values will not change significantly even when the image is taken somewhat out of focus (Model, 2014). Using our imaging system this is indeed the case as the fluorescence is summed within a nuclear boundary determined by the nuclear image (taken at the same focal plane). As an example, Figure 9 shows the average brightness of fluorescently labeled cells as a function of distance from optimal focus at different magnifications. While the fluorescent values drop rapidly when a low DOF 60× lens is used, a 10× lens will allow quantitative fluorescence measurements within about ±5 µm of the best focus.

Photobleaching

Photobleaching of the sample is a major concern in manual imaging, where a single region on the sample may be illuminated with UV (ultraviolet) light for a prolonged time during focusing and scoring. In our system we do not use UV illumination (the DAPI excitation LED has a wavelength of 405 nm) and, with the possible exception of the first frame, do not illuminate any region of the sample for more than a few seconds as fields of view are imaged once for each channel with the illumination turned on immediately before image acquisition.

Using the γ-H2AX assay we have not seen any significant photobleaching of neither DAPI nor the antibody-conjugated fluorophore, even when illuminating the same field of view multiple minutes. We had similar experience with the fluorophores used for the mBAND assay. Using PNA probes, however, we have seen some photobleaching which leads to substantial fading of the centromere fluorescence markers when a field of view was illuminated for a few minutes. In our routine operating conditions this is not a problem as each field of view is only illuminated for a few seconds.

Flatness of Field

The sCMOS camera used provides high resolution through the use of a large (1" diagonal) sensor. As we are using 1" optics in the beam path, it was extremely difficult to provide uniform light collection over such a large area. Figure 10a shows a full sensor image of a uniform brightness test slide (Blue Fluorescence Reference Slide, Ted Pella Inc., Redding, CA). It is evident that brightness varies significantly across the field resulting in big uncertainties in quantitative fluorescence assays like γ-H2AX. This is not an issue for the micronucleus assay or the chromosome based assays, as the nuclei and micronuclei are detected using an adaptive thresholding algorithm and the absolute brightness of each nucleus is not scored.

Two approaches were investigated to overcome this issue. Initially, the sensor was cropped to 1,776 × 1,770 pixels (dashed line in Fig. 10a). Figure 10b shows that this is still not sufficient as nuclei in the corners of the image are very dim and may not be reliably detected. To overcome this problem a gain correction was added to the analysis. This is similar to the approach described by Model (2014) whereas an image of a flat field was taken and the images to be scored were divided by it. As seen in Figure 10c, this

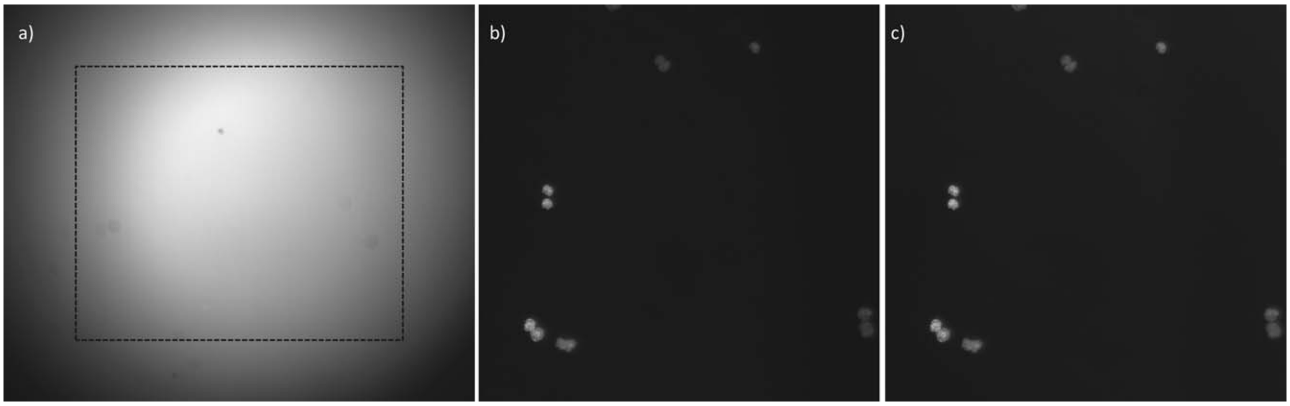

Fig. 10. (**a**) Full frame image of a uniform fluorescence test slide—the dashed line denotes the 1,776 × 1,760 frame used in all images above. (**b**) Image of a field of nuclei (only top right quadrant of image is shown) without gain correction. (**c**) The same image with gain correction. Note that cells in image periphery (top and right) are much brighter than in (b).

works well to equalize cell brightness across the image.

CONCLUSIONS

We described here a versatile and efficient imaging system developed at the Center for High Throughput Minimally Invasive Radiation Biodosimetry at Columbia University. Our goal was to automate the imaging components of several well-known biodosimetry assays. Following the work described in this paper we have put the imaging system into routine use for scoring all four biodosimetry assays described above as part of the ongoing assay optimization and automation work at our center.

ACKNOWLEDGMENTS

The authors acknowledge the continued support of Gary Johnson from the Design and Instrument Shop at the Center for Radiological Research, Columbia University Medical Center. Without him, this work would not be possible. The content is solely the responsibility of the authors and does not necessarily represent the official views of the NIAID or NIH.

REFERENCES

Böcker W, Iliakis G. 2006. Computational methods for analysis of foci: validation for Radiation-induced γ-H2AX foci in human cells. Radiat Res 165:113–124.

Bueno G, Déniz O, Fernández-Carrobles MDM, Vállez N, Salido J. 2014. An automated system for whole microscopic image acquisition and analysis. Microsc Res Tech 77:697–713.

Chen Y, Zhang J, Wang H, Garty G, Xu Y, Lyulko OV, Turner HC, Randers-Pehrson G, Simaan N, Yao YL, Brenner DJ. 2009. Design and preliminary validation of a rapid automated biosodimetry tool for high throughput radiological triage. Proc ASME 3:61–67.

Chen Y, Zhang J, Wang H, Garty G, Xu Y, Lyulko OV, Turner HC, Randers-Pehrson G, Simaan N, Yao YL, Brenner DJ. 2010. Development of a robotically-based automated biodosimetry tool for high-throughput radiological triage. Int J Biomechatronics Biomed Robot 1:115–125.

Chudoba I, Hickmann G, Friedrich T, Jauch A, Kozlowski P, Senger G. 2004. mBAND: a high resolution multicolor banding technique for the detection of complex intrachromosomal aberrations. Cytogenet Genome Res 104:390–393.

da Cruz AD, McArthur AG, Silva CC, Curado MP, Glickman BW. 1994. Human micronucleus counts are correlated with age, smoking, and cesium-137 dose in the Goiania (Brazil) radiological accident. Mutat Res 313:57–68.

Erdogan T. 2011. Optical filters for wavelength selection in fluorescence instrumentation. In: Current protocols in cytometry. Wiley, pp. 2.4.1–2.4.25.

Fenech M. 2007. Cytokinesis-block micronucleus cytome assay. Nat Protoc 2:1084–1104.

Fenech M, Bonassi S, Turner J, Lando C, Ceppi M, Chang WP, Holland N, Kirsch-Volders M, Zeiger E, Bigatti MP, Bolognesi C, Cao J, De Luca G, Di Giorgio M, Ferguson LR, Fucic A, Lima OG, Hadjidekova VV, Hrelia P, Jaworska A, Joksic G, Krishnaja AP, Lee TK, Martelli A, McKay MJ, Migliore L, Mirkova E, Muller WU, Odagiri Y, Orsiere T, Scarfi MR, Silva MJ, Sofuni T, Surralles J, Trenta G, Vorobtsova I, Vral A, Zijno A. 2003. Intra- and inter-laboratory variation in the scoring of micronuclei and nucleoplasmic bridges in binucleated human lymphocytes. Results of an international slide-scoring exercise by the HUMN project. Mutat Res 534:45–64.

Fowler B, Liu C, Mims S, Balicki J, Li W, Do H, Appelbaum J, Vu P. 2010. A 5.5Mpixel 100 frames/sec wide dynamic range low noise CMOS image sensor for scientific applications. Proc. SPIE 7536: 753607-753607-12.

Garty G, Chen Y, Salerno A, Turner H, Zhang J, Lyulko OV, Bertucci A, Xu Y, Wang H, Simaan N, Randers-Pehrson G, Yao YL, Amundson SA, Brenner DJ. 2010. The RABIT: a rapid automated biodosimetry tool for radiological triage. Health Phys 98:209–217.

Garty G, Chen Y, Turner H, Zhang J, Lyulko OV, Bertucci A, Xu Y, Wang H, Simaan N, Randers-Pehrson G, Yao YL, Brenner DJ. 2011. The RABiT: a rapid automated BIodosimetry tool for radiological triage II. Technological developments. Int J Radiat Biol 87: 776–790.

Geusebroek JM, Cornelissen F, Smeulders AWM, Geerts H. 2000. Robust autofocusing in microscopy. Cytometry 39:1–9.

Haney SA, LaPan P, Pan J, Zhang J. 2006. High-content screening moves to the front of the line. Drug Discover Today 11:889–894.

Hou YN, Lavaf A, Huang D, Peters S, Huq R, Friedrich V, Rosenstein BS, Kao J. 2009. Development of an automated gamma-H2AX immunocytochemistry assay. Radiat Res 171:360–367.

International Atomic Energy Agency (IAEA). 2011. Cytogenetic dosimetry: applications in preparedness for and response to radiation emergencies. IAEA emergency preparedness and response series. Vienna: IAEA. pp. 229.

Lee JK, Han E-A, Lee S-S, Ha W-H, Barquinero JF, Lee HR, Cho MS. 2012. Cytogenetic biodosimetry for fukushima travelers after the nuclear power plant accident: no evidence of enhanced yield of dicentrics. J Radiat Res 53:876–881.

Liu XY, Wang WH, Sun Y. 2007. Dynamic evaluation of autofocusing for automated microscopic analysis of blood smear and pap smear. J Microsc (Oxf) 227:15–23.

Lloyd DC, Edwards AA, Moquet JE, Guerrero-Carbajal YC. 2000. The role of cytogenetics in early triage of radiation casualties. Appl Radiat Isotopes 52:1107–1112.

Lyulko OV, Garty G, Randers-Pehrson G, Turner HC, Szolc B, Brenner DJ. 2014. Fast image analysis for the micronucleus assay in a fully automated high-throughput biodosimetry system. Radiat Res 181:146–161.

M'kacher R, Maalouf EEL, Ricoul M, Heidingsfelder L, Laplagne E, Cuceu C, Hempel WM, Colicchio B, Dieterlen A, Sabatier L. 2014. New tool for biological dosimetry: reevaluation and automation of the gold standard method following telomere and centromere staining. Mutat Res 770:45–53.

Mariotti LG, Pirovano G, Savage KI, Ghita M, Ottolenghi A, Prise KM, Schettino G. 2013. Use of the γ-H2AX assay to investigate DNA repair dynamics following multiple radiation exposures. PLoS One 8:e79541.

Model M. 2014. Intensity calibration and flat-field correction for fluorescence microscopes. In: Current protocols in cytometry. Wiley. pp. 10.14.1–10.14.10.

Redon CE, Dickey JS, Bonner WM, Sedelnikova OA. 2009. γ-H2AX as a biomarker of DNA damage induced by ionizing radiation in human peripheral blood lymphocytes and artificial skin. Adv Space Res 43:1171–1178.

Repin M, Turner HC, Garty G, Brenner DJ. 2014. Next generation platforms for high-throughput biodosimetry. Radiat Protect Dosimetry 159:105–110.

Rogan PK, Li Y, Wickramasinghe A, Subasinghe A, Caminsky N, Khan W, Samarabandu J, Wilkins R, Flegal F, Knoll JH. 2014. Automating dicentric chromosome detection from cytogenetic biodosimetry data. Radiat Protect Dosimetry 159:95–104.

Romm H, Ainsbury E, Barnard S, Barrios L, Barquinero JF, Beinke C, Deperas M, Gregoire E, Koivistoinen A, Lindholm C, Moquet J, Oestreicher U, Puig R, Rothkamm K, Sommer S, Thierens H, Vandersickel V, Vral A, Wojcik A. 2013. Automatic scoring of dicentric chromosomes as a tool in large scale radiation accidents. Mutat Res 756:174–183.

Rothkamm K, Löbrich M. 2003. Evidence for a lack of DNA double-strand break repair in human cells exposed to very low X-ray doses. Proc Natl Acad Sci USA 100:5057–5062.

Salerno A, Zhang J, Bhatla A, Lyulko OV, Nie J, Dutta A, Garty G, Simaan N, Randers-Pehrson G, Yao YL, Brenner DJ 2007. Design considerations for a minimally invasive high-throughput automation system for radiation biodosimetry. In *Proceedings of the Third Annual IEEE Conference on Automation Science and Engineering (CASE)*, Scottsdale, AZ, 846–852.

Sharma PM, Ponnaiya B, Taveras M, Shuryak I, Turner H, Brenner DJ. In press. High throughput measurement of γ-H2AX DSB repair kinetics in a healthy human population PLoS ONE 10: e0121083. doi: 10.1371/journal.pone.0121083

Sluder G, Nordberg JJ. 2007. Microscope basics. Greenfield Sluder, Joshua J. Nordberg, Microscope Basics, In: Greenfield S and David E. Wolf, Editor(s). Methods in Cell Biology, Academic Press, 81, pp. 1–10, http://dx.doi.org/10.1016/S0091-679X(06)81001-0.

Suzuki S, Abe K. 1985. Topological structural analysis of digitized binary images by border following. Comput Vis Graph Image Process 29:396.

Turner HC, Brenner DJ, Chen Y, Bertucci A, Zhang J, Wang H, Lyulko OV, Xu Y, Schaefer J, Simaan N, Randers-Pehrson G, Yao YL, Garty G. 2011. Adapting the γ-H2AX assay for automated processing in human lymphocytes. 1. Technological aspects. Radiat Res 175:282–290.

Turner HC, Sharma P, Perrier JR, Bertucci A, Smilenov L, Johnson G, Taveras M, Brenner DJ, Garty G. 2014. The RABiT: high-throughput technology for assessing global DSB repair. Radiat Environ Biophys 53:265–272.

Valente M, Voisin P, Laloi P, Roy L, Roch-Lefèvre S. 2011. Automated gamma-H2AX focus scoring method for human lymphocytes after ionizing radiation exposure. Radiat Meas 46:871–876.

Varga D, Johannes T, Jainta S, Schuster S, Schwarz-Boeger U, Kiechle M, Garcia BP, Vogel W. 2004. An automated scoring procedure for the micronucleus test by image analysis. Mutagenesis 19:391–397.

Wilkins RC, Romm H, Oestreicher U, Marro L, Yoshida MA, Suto Y, Prasanna PGS. 2011. Biological dosimetry by the triage dicentric chromosome assay – further validation of international networking. Radiat Meas 46:923–928.

Zeder M, Pernthaler J. 2009. Multispot Live-image autofocusing for High-throughput microscopy of fluorescently stained bacteria. Cytometry A 75:781–788.